J. Plasma Phys. (2025), *vol*. 91, E157 © The Author(s), 2026. Published by Cambridge University Press.
This is an Open Access article, distributed under the terms of the Creative Commons Attribution licence (https://creativecommons.org/licenses/by/4.0/), which permits unrestricted re-use, distribution and reproduction, provided the original article is properly cited. doi:10.1017/S0022377825101013

Linear stability studies for a quasi-axisymmetric equilibrium including plasma flow, drift and viscosity effects

Erika Strumberger[1], **Jonas Puchmayr**[1] **and Florian Hindenlang**[1]

[1]Max Planck Institute for Plasma Physics, Boltzmannstr. 2, 85748 Garching, Germany

Corresponding author: Erika Strumberger, erika.strumberger@ipp.mpg.de

(Received 29 July 2025; revision received 19 September 2025; accepted 16 October 2025)

Linear stability studies are presented for a quasi-axisymmetric stellarator equilibrium which is unstable with respect to external kink and peeling-ballooning modes. Using the three-dimensional linear stability CASTOR3D code, the effects of parallel viscosity, gyro-viscosity, ion diamagnetic drift velocity, *ExB* velocity and an externally driven flow in direction of the quasi-symmetry are investigated with respect to their influence on growth rate, oscillation frequency and mode structure.

Key words: fusion plasma, plasma flows, plasma instabilities

1. Introduction

Stellarators are again a subject of focus in nuclear fusion research. In particular, their inherent properties, namely steady-state operation and the absence of disruptions, are important requirements for a fusion power plant (Warmer *et al*. 2024). Ongoing optimisation of the magnetic field geometries leads to major improvements of their confinement properties. There are quasi-symmetric (QS) and quasi-isodynamic devices. Using magnetic coordinates (Boozer coordinates (Boozer 1982)), the magnetic field strength of QS stellarators is symmetric in the toroidal direction (quasi-axisymmetric (QA) (Nührenberg *et al*. 1994; Henneberg *et al*. 2019)), in the helical direction (quasi-helically symmetric (Nührenberg & Zille 1988)) or in the poloidal direction (quasi-poloidally symmetric (Spong *et al*. 2005)). Quasi-isodynamic stellarators have no explicit symmetry, but their contours of the magnetic field strength are closed poloidally and the magnetic field is optimised to confine the trapped particles (Goodman *et al*. 2023). However, due to their complex three-dimensional (3-D) geometry, the numerical description of stellarators is much more complicated than for axisymmetric tokamaks. While there are numerous numerical tools to investigate the linear stability properties of tokamaks (e.g. Mars-F (Liu *et al*. 2000), MARS-K (Liu *et al*. 2008), MISHKA-F (Chapman *et al*. 2006), MINERVA-DI (Aiba 2016) etc.), there exists only a limited number for stellarators (e.g. CAS3D (Nührenberg 2021) and TERPSICHORE (Anderson *et al*. 1990)). To our knowledge, the CASTOR3D code (Strumberger & Günter 2017; Strumberger *et al*. 2023)

is the only 3-D linear stability code which includes simultaneously the effects of resistivity, parallel and gyro-viscosity, ion diamagnetic drift velocity, *ExB* velocity and externally driven flows.

The CASTOR3D code has already been successfully applied to external kink modes with low toroidal mode numbers in a QA stellarator configuration including parallel viscosity and toroidal flow (Strumberger & Günter 2019) and to resistive internal kink and double tearing modes in Wendelstein 7-X (Strumberger *et al*. 2020), and diamagnetic effects have been studied for ideal and resistive internal kink modes using simple axisymmetric and 3-D test equilibria (Strumberger *et al*. 2023). CASTOR3D is also used for benchmarks with nonlinear extended magneto-hydrodynamic (MHD) codes (e.g. JOREK (Nikulsin *et al*. 2022; Ramasamy *et al*. 2024) and NIMSTELL (Patil & Sovinec 2024)). While former 3-D CASTOR3D stability calculations were restricted to low toroidal mode numbers, now also stability studies for peeling-ballooning modes in 3-D tokamak (Puchmayr *et al*. 2023, 2024) and stellarator configurations are possible because of increasing memory and computing power, substantial improvement of the performance of the CASTOR3D code (Puchmayr 2023) and last but not least, the use of high fidelity equilibrium solutions computed with the GVEC code (Hindenlang *et al*. 2025*a*).

GVEC is a fixed-boundary 3-D MHD equilibrium solver that follows the same idea as VMEC (Hirshman & Whitson 1983), which is finding a set of nested flux surfaces via an energy minimisation. A distinct feature of GVEC is its radial discretisation with B-splines, thus providing a smooth high-order representation of the equilibrium solution, including the region around the magnetic axis. Furthermore, the coordinate frame to represent the flux surface geometry in GVEC is not restricted to cylindrical coordinates, which enables equilibrium solutions of highly shaped stellarator configurations (Hindenlang *et al*. 2025*b*). GVEC also provides the transformation into Boozer coordinates.

In the following, we present linear stability studies performed for a QA, high plasma-β equilibrium which is unstable with respect to ideal external modes from low up to high toroidal mode numbers. This two-periodic stellarator equilibrium was already used for previous CASTOR3D stability studies described in detail in Strumberger & Günter (2019). Yet, at that time our computations were limited to $n_{tot} = 7$ and $m_{tot} = 13$ per n, with n_{tot} and m_{tot} being the total numbers of toroidal and poloidal Fourier harmonics which could be used simultaneously. Therefore, we could only investigate external kink modes with low toroidal mode numbers taking into account parallel viscosity and toroidal flow. However, drift effects and the *ExB* velocity were not included in this older code version. We choose again this equilibrium because of its numerous and strong instabilities ranging from external kink to peeling-ballooning modes. We will study the effects of parallel viscosity, gyro-viscosity, ion diamagnetic drift velocity, *ExB* velocity and an externally driven flow in the direction of the quasi-symmetry with respect to their influence on the growth rate, oscillation frequency and mode structure of these external modes.

In § 2, we present the linearised extended MHD equations which are used for the computations. The stability studies are the subject of § 3. We start with ideal stability studies in § 3.1. The effects of parallel viscosity and gyro-viscosity are discussed in § 3.2, while the effects of ion diamagnetic velocity, *ExB* velocity and an externally driven flow are investigated in § 3.3. In § 4, a summary of the results is given. Finally, the definition of the eigenfunctions and the determination of stellarator mode types is described in the appendix.

https://doi.org/10.1017/S0022377825101013 Published online by Cambridge University Press

2. Linearised extended MHD equations

In this section, we briefly summarise the equations and definitions which are the basis of the presented stability studies. They are described in more detail in Strumberger *et al*. (2023).

The linearised extended MHD equations including parallel and gyro-viscosity, ion diamagnetic drift velocity, *ExB* velocity and additional poloidal and toroidal velocity terms read

$$\lambda\rho_1 = -\boldsymbol{V}_0\cdot\nabla\rho_1 - \boldsymbol{V}_1\cdot\nabla\rho_0 - \rho_1\nabla\cdot\boldsymbol{V}_0 - \rho_0\nabla\cdot\boldsymbol{V}_1, \tag{2.1}$$

$$\begin{aligned}\rho_0\lambda\boldsymbol{V}_1 = &-\rho_1(\boldsymbol{V}_0\cdot\nabla)\boldsymbol{V}_0 - \rho_0(\boldsymbol{V}_1\cdot\nabla)\boldsymbol{V}_0 - \rho_0(\boldsymbol{V}_0\cdot\nabla)\boldsymbol{V}_1\\ &+\rho_1(\boldsymbol{V}^*_{i0}\cdot\nabla)\boldsymbol{V}_0 + \rho_0(\boldsymbol{V}^*_{i1}\cdot\nabla)\boldsymbol{V}_0 + \rho_0(\boldsymbol{V}^*_{i0}\cdot\nabla)\boldsymbol{V}_1\\ &-\frac{1}{m_i}\nabla(\rho_0 T_1) - \frac{1}{m_i}\nabla(T_0\rho_1) + \mu_{||}\Delta_{||}\boldsymbol{V}_1\\ &+\frac{1}{\mu_0}(\nabla\times(\nabla\times\boldsymbol{A}_1))\times(\nabla\times\boldsymbol{A}_0)\\ &+\frac{1}{\mu_0}(\nabla\times(\nabla\times\boldsymbol{A}_0))\times(\nabla\times\boldsymbol{A}_1),\end{aligned} \tag{2.2}$$

$$\lambda T_1 = -\boldsymbol{V}_1\cdot\nabla T_0 - \boldsymbol{V}_0\cdot\nabla T_1 - (\Gamma-1)T_1\nabla\cdot\boldsymbol{V}_0 - (\Gamma-1)T_0\nabla\cdot\boldsymbol{V}_1, \tag{2.3}$$

$$\lambda\boldsymbol{A}_1 = \boldsymbol{V}_1\times\boldsymbol{B}_0 + \boldsymbol{V}_0\times(\nabla\times\boldsymbol{A}_1). \tag{2.4}$$

Here, ρ_0, $\boldsymbol{V}_0$, T_0, $\boldsymbol{A}_0$ are the equilibrium quantities of density, velocity, temperature ($T_0 = T_{0e} + T_{0i}$) and magnetic vector potential, while ρ_1, $\boldsymbol{V}_1$, T_1, $\boldsymbol{A}_1$ are their perturbations. The perturbation of the ion diamagnetic drift velocity (2.6) reads

$$\begin{aligned}\boldsymbol{V}^*_{i1} = &-\alpha\alpha_T\frac{\rho_1}{\rho_0^2}\frac{\boldsymbol{B}_0\times\nabla p_0}{B_0^2} + \alpha\alpha_T\frac{1}{\rho_0}\frac{\boldsymbol{B}_0\times(T_0\nabla\rho_1 + T_1\nabla\rho_0 + \rho_0\nabla T_1 + \rho_1\nabla T_0)}{B_0^2}\\ &+\alpha\alpha_T\frac{1}{\rho_0}\frac{(\nabla\times\boldsymbol{A}_1)\times\nabla p_0}{B_0^2} - 2\alpha\alpha_T\frac{1}{\rho_0}\frac{\boldsymbol{B}_0\cdot(\nabla\times\boldsymbol{A}_1)}{B_0^4}(\boldsymbol{B}_0\times\nabla p_0).\end{aligned} \tag{2.5}$$

The time dependence of the perturbed quantities is taken to be $\sim e^{\lambda t}$ with eigenvalue $\lambda = \gamma + i\omega$. The real part of λ corresponds to the growth rate γ, while ω is the oscillation frequency of the perturbation.

These equations correspond to the generally used linearised single-fluid equations (e.g. Huysmans, Goedbloed & Kerner 1993) plus additional two-fluid terms. They are derived from the two-fluid MHD equations (Braginskii 1965) making several assumptions and approximations, e.g. assuming quasi-neutrality $n = n_i = n_e$ ($n_i =$ ion density, $n_e =$ electron density), neglecting the electron mass m_e ($m_i >> m_e$, mass density $\rho = m_i n + m_e n \approx m_i n$) and using the pressure $p = p_i + p_e = n(T_i + T_e) = nT$ ($T_i =$ ion temperature, $T_e =$ electron temperature). The unperturbed velocity $\boldsymbol{V}_0$ corresponds to the ion velocity

$$\boldsymbol{V}_0 = \boldsymbol{V}_{i0} = \underbrace{\frac{\boldsymbol{E}_0\times\boldsymbol{B}_0}{B_0^2}}_{=\boldsymbol{V}_{ExB}} + \underbrace{\alpha\frac{1}{\rho_0}\frac{\boldsymbol{B}_0\times\nabla p_{i0}}{B_0^2}}_{=\boldsymbol{V}^*_{i0}} + \boldsymbol{V}^{ext}. \tag{2.6}$$

https://doi.org/10.1017/S0022377825101013 Published online by Cambridge University Press

Here, $\boldsymbol{V}_{ExB} + \boldsymbol{V}^*_{i0}$ are the ExB flow and the ion diamagnetic drift velocity with $\boldsymbol{E}_0$ and $\boldsymbol{B}_0$ being the electric and magnetic fields, and $\alpha = m_i/e$ with m_i and e being the ion mass and elementary charge. Here, we neglect the parallel velocity, but we take into account an externally driven flow $\boldsymbol{V}^{ext}$, e.g. caused by neutral beam injection. Furthermore, the considered equations contain the linearised forms of the parallel viscous force density $-\boldsymbol{\nabla}\cdot\boldsymbol{\Pi}_{||} = \mu_{||}\Delta_{||}\boldsymbol{V}$[1] with $\mu_{||}$ being the parallel viscosity coefficient, and the gyro-viscous force density being approximated by $-\boldsymbol{\nabla}\cdot\boldsymbol{\Pi}_{\wedge} \approx \rho(\boldsymbol{V}^*_i\cdot\boldsymbol{\nabla})\boldsymbol{V}$ (Chang & Callen 1992). Since, we consider single-fluid equations, but T_i and T_e may be different, we use

$$T_i = \alpha_T T \quad \text{and} \quad T_e = (1-\alpha_T)T \quad \text{with} \quad 0 \leqslant \alpha_T \leqslant 1. \tag{2.7}$$

The parameter α_T provides an additional degree of freedom that allows us to choose a more realistic ratio of ion and electron pressures with respect to the measured temperatures. The coefficients Γ and μ_0 denote the adiabtic index ($\Gamma = 5/3$) and the vacuum permeability.

3. Linear stability studies

As already mentioned, the two-periodic, QA equilibrium described in Strumberger & Günter (2019) is used for the following stability studies. Its high volume-averaged plasma beta of $\langle\beta\rangle = 2.9\,\%$ together with the flat safety factor profile $q(s)$ in the boundary region (boundary value $q_b = 1.79$, see figure 1*b*) make it unstable with respect to ideal external kink and peeling-ballooning modes. Since, highly accurate equilibria are the basis for the ambitious stability studies presented below, we recalculated the equilibrium with the 3-D equilibrium code GVEC (Hindenlang *et al.* 2025*a*) and used its transformation into Boozer coordinates. For the equilibrium calculation with GVEC, we used 20 toroidal and 18 poloidal Fourier harmonics and 300 radial elements with a polynomial degree of the radial B-splines of 5. The transformation into Boozer coordinates has been calculated with GVEC using 80 toroidal and 72 poloidal Fourier harmonics in the new Boozer coordinate system. While we simply used a constant density in the previous stability studies, we now use a density profile ($\rho_0 = m_i n_a(1-0.8s^4)$, $n_a = 4\times10^{19}\,\mathrm{m}^{-3}$, m_i = deuteron mass). The latter leads to higher growth rates because of the reduced inertia in the boundary region. Figure 1(*c*) shows the normalised profiles of density and temperature.

Boozer magnetic flux coordinates (s, v, u) are advantageous for 3-D stability studies because magnetic field lines are straight in these coordinates (Boozer 1982). Figure 1(*a*) illustrates the toroidal v and poloidal u coordinate lines at the plasma boundary of the QA equilibrium while the square root of the normalised toroidal flux serves as the radial coordinate s. Using these coordinates, the ion diamagnetic drift velocity reads

$$\boldsymbol{V}^*_{i0} = \frac{m_i}{e}\frac{1}{\rho_0}\frac{\boldsymbol{B}_0\times\boldsymbol{\nabla}p_{i0}}{B_0^2}$$

$$= \frac{m_i}{e}\frac{1}{\rho_0}\frac{\partial p_{i0}}{\partial s}\left(\frac{I}{\Phi' J + \Psi' I}\boldsymbol{r}_{,v} - \frac{J}{\Phi' J + \Psi' I}\boldsymbol{r}_{,u}\right) = \frac{1}{2\pi}\Omega^{i*}_{tor}\boldsymbol{r}_{,v} + \frac{1}{2\pi}\Omega^{i*}_{pol}\boldsymbol{r}_{,u}, \tag{3.1}$$

[1] Up to now, the perpendicular viscous force $\boldsymbol{\nabla}\cdot\boldsymbol{\Pi}_{\perp}$ resulting also from the viscous stress tensor $\boldsymbol{\Pi} = \boldsymbol{\Pi}_{||} + \boldsymbol{\Pi}_{\wedge} + \boldsymbol{\Pi}_{\perp}$ is not implemented in CASTOR3D.

https://doi.org/10.1017/S0022377825101013 Published online by Cambridge University Press

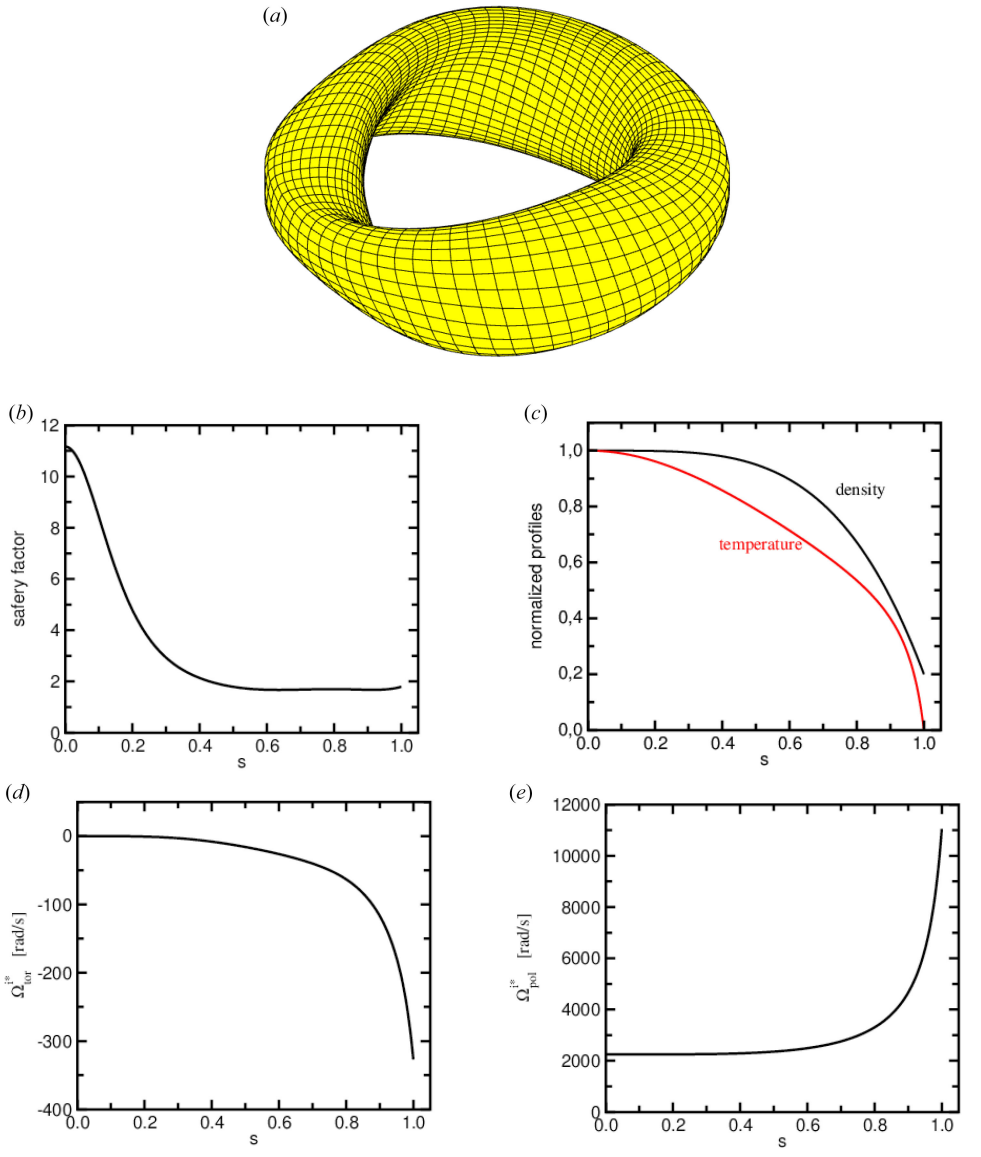


FIGURE 1. (*a*) Poloidal and toroidal coordinate lines in Boozer coordinates at the plasma boundary ($s = 1$) of the QA equilibrium. (*b*) Safety factor, (*c*) normalised density and temperature profiles, (*d*) toroidal and (*e*) poloidal ion drift frequencies (3.2) as functions of the square root of the normalised toroidal flux s.

with

$$\Omega^{i*}_{tor}(s) = 2\pi \frac{m_i}{e} \frac{1}{\rho_0} \frac{\partial p_{i0}}{\partial s} \frac{I}{\Phi' J + \Psi' I} \quad \text{and} \quad \Omega^{i*}_{pol}(s) = -2\pi \frac{m_i}{e} \frac{1}{\rho_0} \frac{\partial p_{i0}}{\partial s} \frac{J}{\Phi' J + \Psi' I} \tag{3.2}$$

being constant on flux surfaces. Here, $I(s)$ and $J(s)$ are the total toroidal and poloidal currents, while Φ' and Ψ' are the derivatives of the toroidal $\Phi(s)$ and poloidal $\Psi(s)$ fluxes. The toroidal $\Omega^{i*}_{tor}(s)$ and poloidal $\Omega^{i*}_{pol}(s)$ drift frequencies are

https://doi.org/10.1017/S0022377825101013 Published online by Cambridge University Press

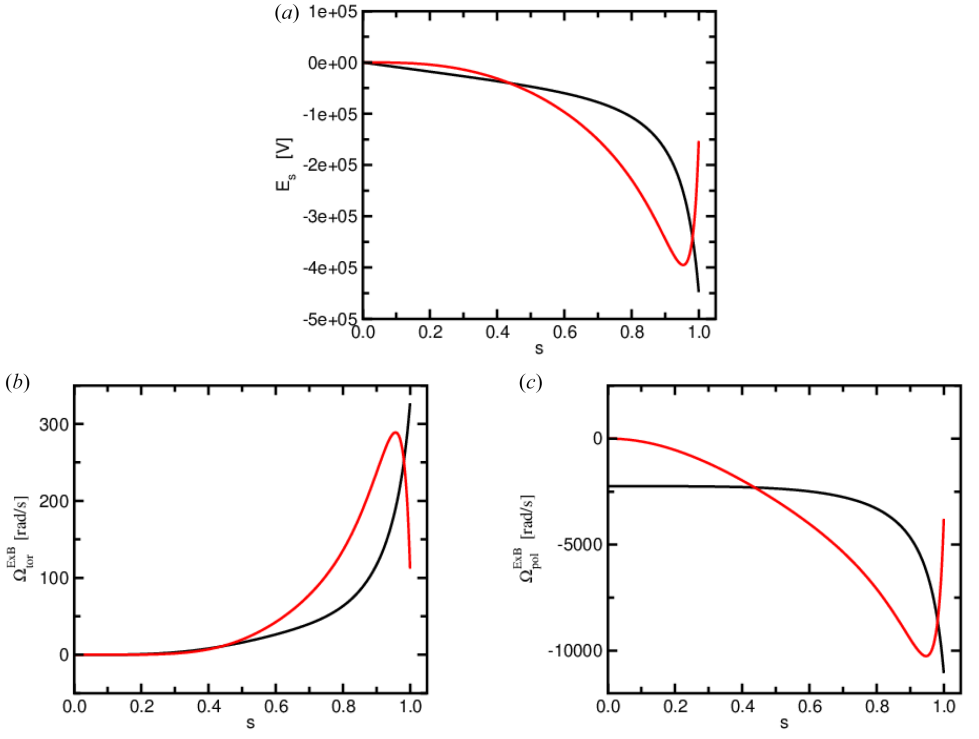


FIGURE 2. (*a*) Co-variant component of the radial electric field using the ambipolarity condition (3.5) (black) and a hypothetical function (red), and the resulting (*b*) toroidal and (*c*) poloidal frequency profiles (3.4) as functions of s.

shown in figures 1(*d*) and 1(*e*). As expected, the poloidal frequency is much larger than the toroidal one ($J \gg I$).

We implemented the *E*x*B* velocity in the CASTOR3D code assuming that the electric potential Φ_E is constant on flux surfaces, that is,

$$\boldsymbol{E}_0 = -\frac{\partial \Phi_E}{\partial s}\nabla s = E_s \nabla s, \tag{3.3}$$

with E_s being the radial co-variant component. This assumption excludes radial flows which would be generated by non-radial components of $\boldsymbol{E}_0$. Analogous to the ion diamagnetic drift velocity (3.1), we obtain in Boozer coordinates

$$\boldsymbol{V}_{ExB} = \frac{\boldsymbol{B}_0 \times \nabla \Phi_E(s)}{B_0^2} = \frac{1}{2\pi}\Omega_{tor}^{ExB}\boldsymbol{r}_{,v} + \frac{1}{2\pi}\Omega_{pol}^{ExB}\boldsymbol{r}_{,u}. \tag{3.4}$$

Assuming $T_{i0} \approx T_{e0}$, that is, $\alpha_T = 0.5$ (2.7) and $\hat{\nu}_i/\sqrt{m_i} \approx \hat{\nu}_e/\sqrt{m_e}$ ($\hat{\nu}_i$ and $\hat{\nu}_e$ are the ion and electron collision frequencies normalised to the corresponding particle masses with $m_i \ll m_e$), the well-known ambipolarity condition (Stroth, Manz & Ramisch 2011; Viezzer 2012) simplifies to

$$E_s \approx \frac{m_i}{e}\frac{1}{\rho_0}\frac{\partial p_{i0}}{\partial s}, \tag{3.5}$$

represented by the black curve in figure 2(*a*). In this case, the ion diamagnetic drift velocity is balanced by the *E*x*B* velocity. The red curve shows a hypothetical profile

https://doi.org/10.1017/S0022377825101013 Published online by Cambridge University Press

of E_s which, in combination with the ion diamagnetic drift velocity, leads to a finite velocity. Usually, E_s will be provided by experimental measurements, however, such a profile is not available for our quasi-axisymmetric test equilibrium. Figures 2(*b*) and 2(*c*) show the corresponding toroidal and poloidal frequency profiles of the *ExB* velocity obtained from the two types of E_s presented in figure 2(*a*). Again, the poloidal frequency is much larger than the toroidal one because $J \gg I$. However, analogous to a tokamak, a plasma of a QA stellarator enjoys 'intrinsic ambipolarity' and is free to rotate in the direction of symmetry (Helander & Simakov 2008) which corresponds to the toroidal direction (v-direction) in Boozer coordinates. That is, neutral beam injection, lower hybrid waves, etc. may drive a fast toroidal rotation. We use a hypothetical toroidal rotation profile with $\Omega_{tor}^{ext} = \Omega_0(1 - 0.8s^4)$ to study the combined effects of parallel viscosity, gyro-viscosity, the velocities $\boldsymbol{V}_{i0}^*$ and $\boldsymbol{V}_{ExB}$ and an externally driven toroidal flow $\boldsymbol{V}^{ext} = (1/2\pi)\Omega_{tor}^{ext}\boldsymbol{r}_{,v}$ in § 3.3.

3.1. *Ideal external modes*

We start the stability studies with the pure ideal MHD equations, that is, without taking viscosity, drift effects or plasma flow into account. While modes of axisymmetric tokamak equilibria are characterised by their toroidal mode number n, several toroidal harmonics couple in the case of a 3-D plasma configuration. We, therefore, introduced the toroidal mode number n^* (Strumberger & Günter 2019) to characterise the modes, with n^* being the dominant toroidal harmonic contributing to the Fourier spectrum of the mode. While in the case of low-n^* modes n^* can be easily identified by regarding the Fourier spectra of the eigenfunctions (figures 3*b* and 3*c*), this method becomes very difficult (figure 3*d*) or even impossible for high-n^* modes (figure 3*e*). For this reason, we compute the contributions of the Fourier harmonics in dependence on n and then determine the n value with the maximum contribution (for details see appendix, equations (A5) and (A6)). Yet, even this method does not always yield distinct results, as shown in the subsequent sections.

Figure 3(*a*) presents the growth rates γ of ideal external modes as functions of n^*. The fluctuations of γ result from the varying distances of the mode relevant rational surfaces from the plasma boundary. These fluctuations are largest for small n^* and decrease with increasing mode number. Disregarding the fluctuations, the growth rates increase with rising n^*, that is, the high-n^* peeling-ballooning modes are more unstable than the low-n^* external kink modes. Because of the two-periodic geometry of the equilibrium, there exist two mode families, namely the so-called odd ($n = 1,3,5,\ldots$) and even ($n = 0,2,4,6,\ldots$) mode families. Only the harmonics of a mode family couple together (Nührenberg 1996). The eigenfunctions (A1) couple to pure sine- and cosine-type functions with specific locations because of the stellarator symmetry of the QA equilibrium. Figures 3(*b*) and 3(*c*) show the Fourier coefficients of the radial velocity perturbation as functions of s (A4) for the $n^* = 4$ external kink modes. Here, $\hat{v}_{mn}^s$ and $\hat{\hat{v}}_{mn}^s$ are exactly equal with opposite (sine-type) and equal signs (cosine-type), respectively. This holds for both the real and (not shown) imaginary parts, while the signs and amplitudes of real and imaginary parts may be different (see appendix). The growth rates of the two modes are slightly different, that is, one location promotes the growth of the mode more than the other. Here, growth rates of sine- and cosine-type modes are clearly non-degenerate for $n^* \leqslant 6$ with $|\Delta\gamma| \geqslant 1\,\%$. These modes are locked to their positions, that is, plasma flow has to exceed a critical value to unlock them. The critical value decreases with $\Delta\gamma$ and becomes zero for degenerate growth rates (Strumberger & Günter 2019; Puchmayr *et al*. 2023).

https://doi.org/10.1017/S0022377825101013 Published online by Cambridge University Press

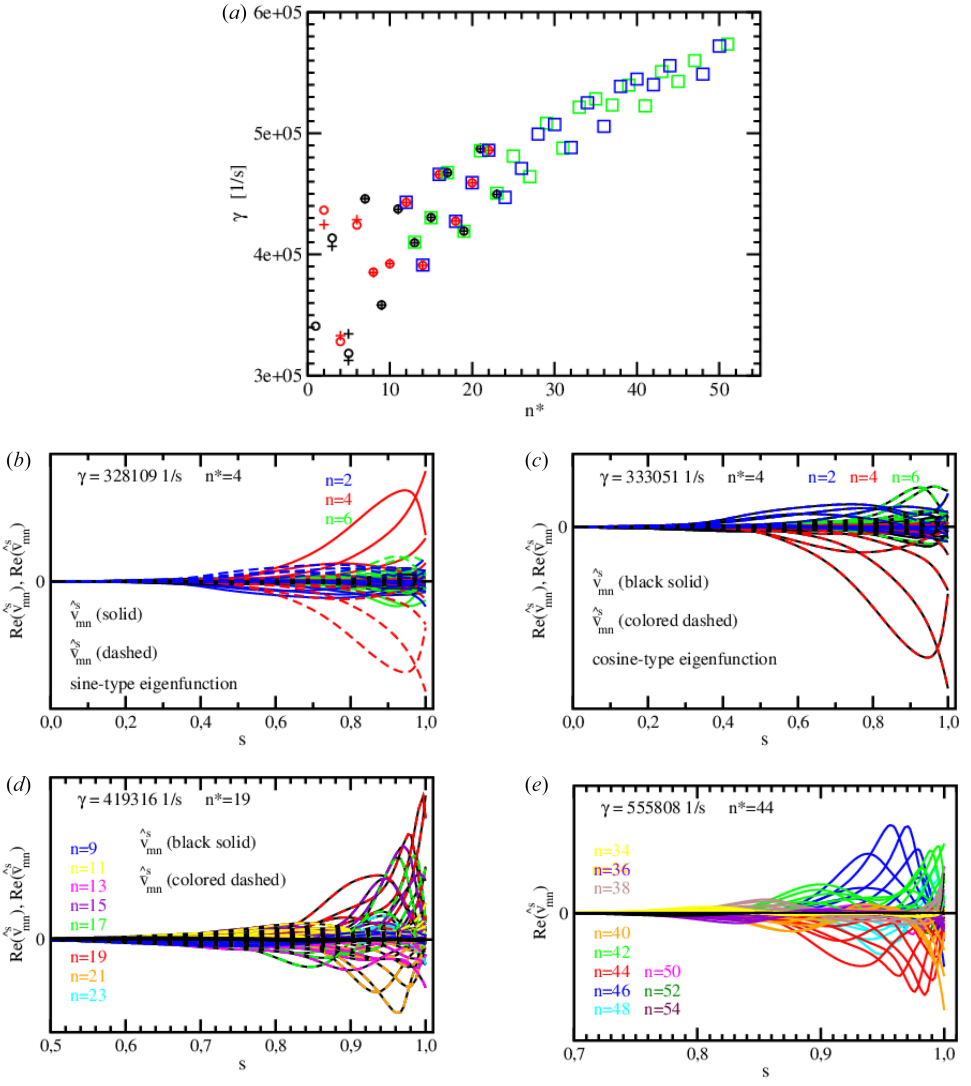


FIGURE 3. (*a*) Growth rate as function of the dominating toroidal mode number n^* for an ideal equilibrium. The results are subdivided into odd (black and green) and even (red and blue) mode families, and into full- (black and red) and reduced-size (green and blue) calculations. The results of the full-size calculations are marked by circles (sine-type solutions) and plus symbols (cosine-type solutions). (*b*)–(*e*) Eigenfunction Fourier spectra of the radial velocity perturbation for (*b*) sine-type and (*c*) cosine-type $n^* = 4$ external kink modes, (*d*) a cosine-type $n^* = 19$ and (*e*) an $n^* = 44$ peeling-ballooning mode. The latter has been computed using the reduced-size eigenvalue problem.

Even in cases where the growth rates are equal within the numerical accuracy, the stellarator symmetry leads to sine- and cosine-type eigenfunctions, as shown for a cosine-type $n^* = 19$ mode in figure 3(*d*). The ideal 3-D CAS3D code is able to exploit the stellarator symmetry and to separate the eigenvalue problem into sine- and cosine-type solutions (Nührenberg 1996, 2016), while the CASTOR3D code solves a complex eigenvalue problem based on complex and complex-conjugate exponential

https://doi.org/10.1017/S0022377825101013 Published online by Cambridge University Press

functions (A1). However, when the coupling between the two parts no longer plays a role, which implies that the growth rates are degenerate, the ansatz for the eigenfunctions (A1) and with it the size of the eigenvalue problem can be reduced considerably by neglecting the complex-conjugate exponential function part (A3). The reduction of the matrix size by a factor of four leads to an important reduction of memory and computational time, so that the number of included poloidal and toroidal harmonics and/or the number of radial grid points can be increased accordingly. This increase is essential to achieve a sufficient numerical accuracy for the computation of high-n^* peeling-ballooning modes. Performing the full- and the reduced-size eigenvalue problems under the same conditions for intermediate n^*-values, we obtain the same eigenvalues as shown in figure 3(*a*). Figure 3(*e*) shows the Fourier spectrum of the radial velocity perturbation of an $n^* = 44$ peeling-ballooning mode computed with the reduced-size eigenvalue problem.

3.2. *Parallel and gyro-viscosity*

In a first step, we consider only the parallel viscosity. Using a rough estimate of the parallel viscosity coefficient[2] (Strumberger & Günter 2019), we get $1 \lesssim \mu_{||} \lesssim 10\,\mathrm{kg\,ms^{-1}}$.

In figure 3(*a*), which shows the ideal growth rates without viscosity, there are growth rates for two cosine-type $n^* = 5$ modes, while the value of the cosine-type $n^* = 1$ mode is missing. Comparing, on the contrary, the growth rates of the $n^* = 1$ and the $n^* = 5$ modes, it seems reasonable to assign the more unstable cosine-type $n^* = 5$ mode to the sine-type $n^* = 1$ mode. Turning on the parallel viscosity confirms that this assignment is justified. Figure 4(*a*) presents the normalised functions $f_{Re}(n)$ and $\bar{f}_{Re}(n)$ (A5) for various parallel viscosity coefficients $\mu_{||}$. As explained in the appendix, the maxima of these functions define the most contributing toroidal Fourier harmonic n^*. This maximum value changes from $n^* = 5$ to $n^* = 1$ in the range of $2 < \mu_{||} < 3\,\mathrm{kg\,ms^{-1}}$. That is, the parallel viscosity has not only a stabilising effect, as shown in figure 4(*b*), but it can also change the structure of the mode and its n^*-type. Nevertheless, the modes are still sine- and cosine-type modes, respectively.

The growth rates of external kink and peeling-ballooning modes with and without parallel viscosity are compared in figure 4(*b*). The damping effect of the parallel viscosity increases with n^*. The peeling-ballooning modes are clearly less unstable if a viscosity of $\mu_{||} = 4\,\mathrm{kg\,ms^{-1}}$ is included. Yet, the high-n^* peeling-ballooning modes are still more unstable than the low-n^* external kink modes.

Since the damping of the growth rate depends on the mode type, the lines representing the growth rates of the sine- and cosine-type $n^* = 9$ modes intersect the lines of the $n^* = 1$ modes in figure 4(*c*). In these intersection regions the sine-type $n^* = 1$ and $n^* = 9$ modes ($1 < \mu_{||} < 1.3\,\mathrm{kg\,ms^{-1}}$) and the cosine-type $n^* = 1$ and $n^* = 9$ modes ($3.4 < \mu_{||} < 4.1\,\mathrm{kg\,ms^{-1}}$) couple to oscillating overstable modes which oscillate between the $n^* = 1$ and $n^* = 9$ types, as figures 4(*e*) and 4(*f*) illustrate. Here, the real and the imaginary parts of the eigenfunction Fourier spectrum are presented for the radial velocity perturbation of the sine-type overstable mode. The real part corresponds to the $n^* = 9$ mode, while the imaginary part represents the $n^* = 1$ mode. The resulting perturbation multiplied with the eigenvalue describes a growing mode oscillating between the $n^* = 9$ and $n^* = 1$ state. The oscillation frequencies of the overstable modes are illustrated in figure 4(*d*). In axisymmetric equilibria an

[2]Here, $\mu_{||} \approx \kappa_{||} v_i^{th} \rho_a / k_{||}$, with $\kappa_{||} \sim \sqrt{\pi}$, wave vector $k_{||} \sim 1/R_0$ ($R_0 = 12.29$ m), density $\rho_a \sim 10^{-7}\,\mathrm{kg\,m^{-3}}$ and ion thermal velocity $v_i^{th} \sim 10^6\,\mathrm{m\,s^{-1}}$.

https://doi.org/10.1017/S0022377825101013 Published online by Cambridge University Press

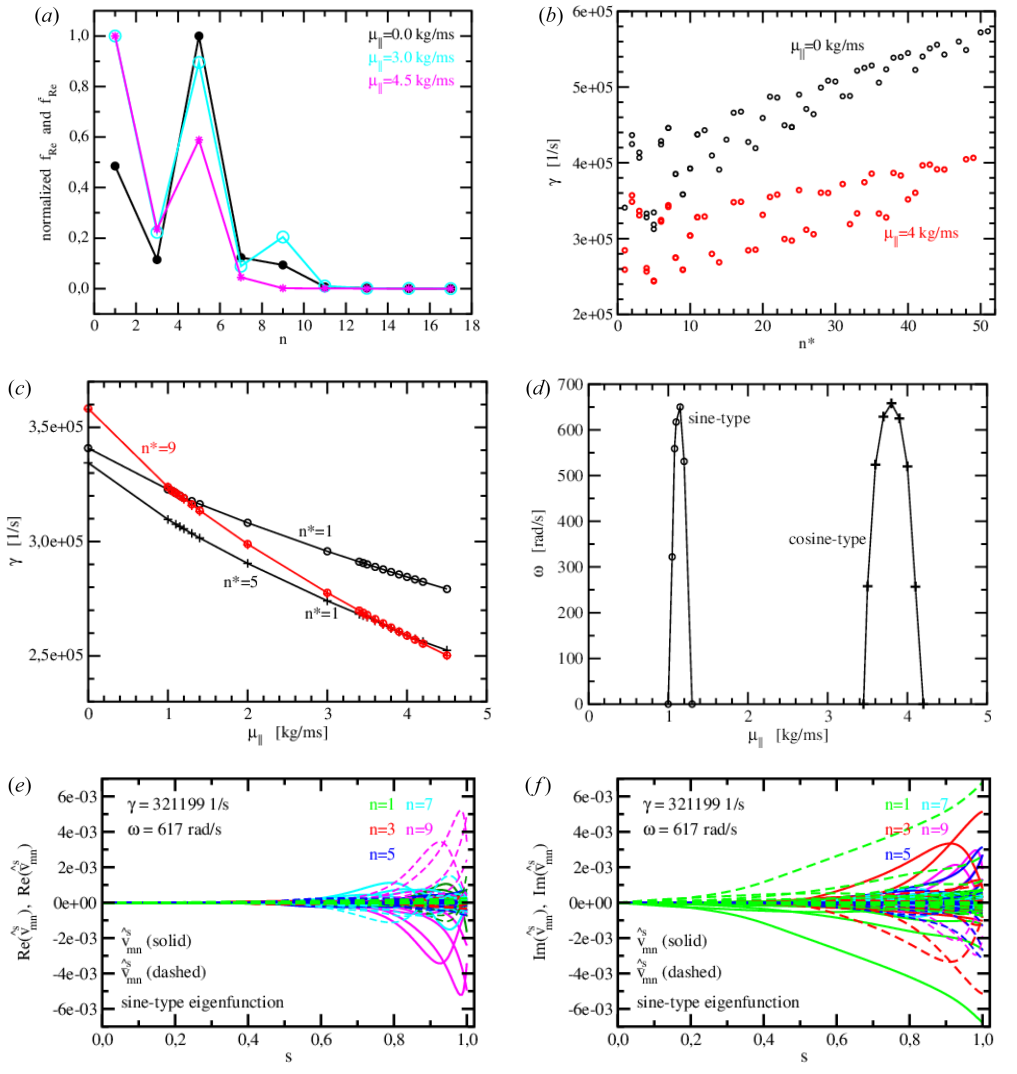


FIGURE 4. (*a*) Contributions of the toroidal Fourier harmonics (f_{RE} (solid lines), $\bar{f}_{RE}$ (symbols)) to the $n^* = 1/n^* = 5$ cosine-type mode for various values of the parallel viscosity coefficient $\mu_{||}$. (*b*) Growth rates as functions of n^* without (black circles) and with (red circles) taking parallel viscosity into account. (*c*) Growth rates as functions of the dynamic viscosity coefficient $\mu_{||}$ for $n^* = 1$ and $n^* = 9$ sine-type (circles) and cosine-type (plus symbols) modes. (*d*) Oscillation frequencies of the sine-type and cosine-type $n^* = 1 \leftrightarrow n^* = 9$ overstable modes. (*e*) Real and (*f*) imaginary parts of the eigenfunction Fourier spectrum for the radial velocity perturbation of the sine-type overstable mode ($\mu_{||} = 1.1\,\mathrm{kg\,ms^{-1}}$).

overstable mode may occur if at least two unstable modes of the same n-type exist and their growth rates overlap within certain ranges of plasma parameters. When the growth rates as functions of a single parameter (e.g. pressure gradient (Kerner, Jakoby & Lerbinger 1986), resistivity (Huysmans *et al*. 1993), etc.) become the same, an overstable oscillating mode evolves. However, the toroidal harmonics are coupled in 3-D equilibria. Therefore, overstable modes can also evolve if the growth rates of

https://doi.org/10.1017/S0022377825101013 Published online by Cambridge University Press

any n^*-modes of the same mode family overlap within a certain parameter range (Strumberger *et al*. 2020). The occurrence of overstable modes strongly depends on the equilibrium parameters (Kerner *et al*. 1986). Our computations confirm that the effect disappears for slightly different parameters.

Assuming that there is no external flow drive and that the ambipolarity condition (3.5) holds ($\boldsymbol{V}_{ExB} = -\boldsymbol{V}^*_{i0}$), all terms containing $\boldsymbol{V}_0$ disappear in the linearised MHD equations (2.1)–(2.4), and the linearised momentum equation (2.2) reads

$$\rho_0 \lambda \boldsymbol{V}_1 = -\frac{1}{m_i}\nabla(\rho_0 T_1) - \frac{1}{m_i}\nabla(T_0 \rho_1) + \rho_0(\boldsymbol{V}^*_{i0}\cdot\nabla)\boldsymbol{V}_1 + \mu_{||}\Delta_{||}\boldsymbol{V}_1 + \frac{1}{\mu_0}(\nabla\times(\nabla\times\boldsymbol{A}_1))\times(\nabla\times\boldsymbol{A}_0) + \frac{1}{\mu_0}(\nabla\times(\nabla\times\boldsymbol{A}_0))\times(\nabla\times\boldsymbol{A}_1). \tag{3.6}$$

While the parallel viscosity only reduces the growth rate, but does not cause mode oscillations,[3] the gyro-viscosity term leads to oscillations. Assuming a parallel viscosity of $\mu_{||} = 4\,\mathrm{kg\,ms^{-1}}$, the gyro-viscosity decouples the $n^* = 1$, $n^* = 9$ cosine-type overstable mode already if only $\approx$1 % of its nominal amplitude is taken into account ($\alpha_s > 0.01$).[4] The remaining $n^* = 1$ cosine-type mode stops oscillation, while the growth rates of the cosine- and sine-type $n^* = 9$ become equal and start to oscillate in the range of $0.05 < \alpha_s < 0.075$. However, even the full gyro-viscosity term ($\alpha_s = 1$) is not strong enough to unlock the $n^* = 1$ modes of the considered plasma configuration, whereas all instabilities with $n^* > 1$ unlock and oscillate. As an example, figures 5(*a*) and 5(*b*) show the behaviour of the $n^* = 2$ modes as a function of α_s. The initially non-degenerate growth rates converge until they become equal for $\alpha_s \lesssim 0.77$. At that point the modes unlock and start to oscillate. Figure 5(*c*) illustrates the growth rates and oscillation frequencies as functions of n^* if parallel and gyro-viscosity are taken into account. Furthermore, the growth rates with parallel but without gyro-viscosity are shown to depict the small additional stabilising effect of the gyro-viscosity. Again the stabilising effect increases with n^*, so that now the $n^* = 2$ external kink mode becomes the most unstable mode in the considered range of n^*-values.

The gyro-viscosity not only equals the otherwise non-degenerate low-n^* eigenvalues (besides $n^* = 1$), but also destroys the sine and cosine-type characters of the stellarator instabilities. Figure 5(*d–g*) show the real and imaginary parts of the radial velocity perturbation for the $n^* = 3$ and the $n^* = 9$ external kink modes. These spectra do not show the typical sine or cosine-type structure of ideal stellarator modes. In the case of the $n^* = 3$ mode the Fourier spectra are dominated by the Fourier coefficients $\hat{\tilde{v}}^s_{mn}$, while there is only as small contribution from the $\hat{v}^s_{mn}$ coefficients. Depending on the sign of the oscillation frequency, the contributions of $\hat{\tilde{v}}^s_{mn}$ or $\hat{v}^s_{mn}$ are negligibly small for high-n^* modes. Solving the full eigenvalue problem, we always get two oscillating solutions with $\gamma_1 = \gamma_2$ and $\omega_1 = -\omega_2$ (see also Strumberger & Günter 2019). Here, the solutions with $\omega > 0$ and $\omega < 0$ are dominated by Fourier harmonics of the complex and complex-conjugate exponential functions, respectively. Thus, both solutions describe the same oscillation of the instability.

[3]The oscillations of overstable modes are a result of equal eigenvalues of two different modes.

[4]The scaling factor α_s has been implemented into the CASTOR3D code to vary $\boldsymbol{V}^*_{i0}$ between zero and its nominal amplitude.

https://doi.org/10.1017/S0022377825101013 Published online by Cambridge University Press

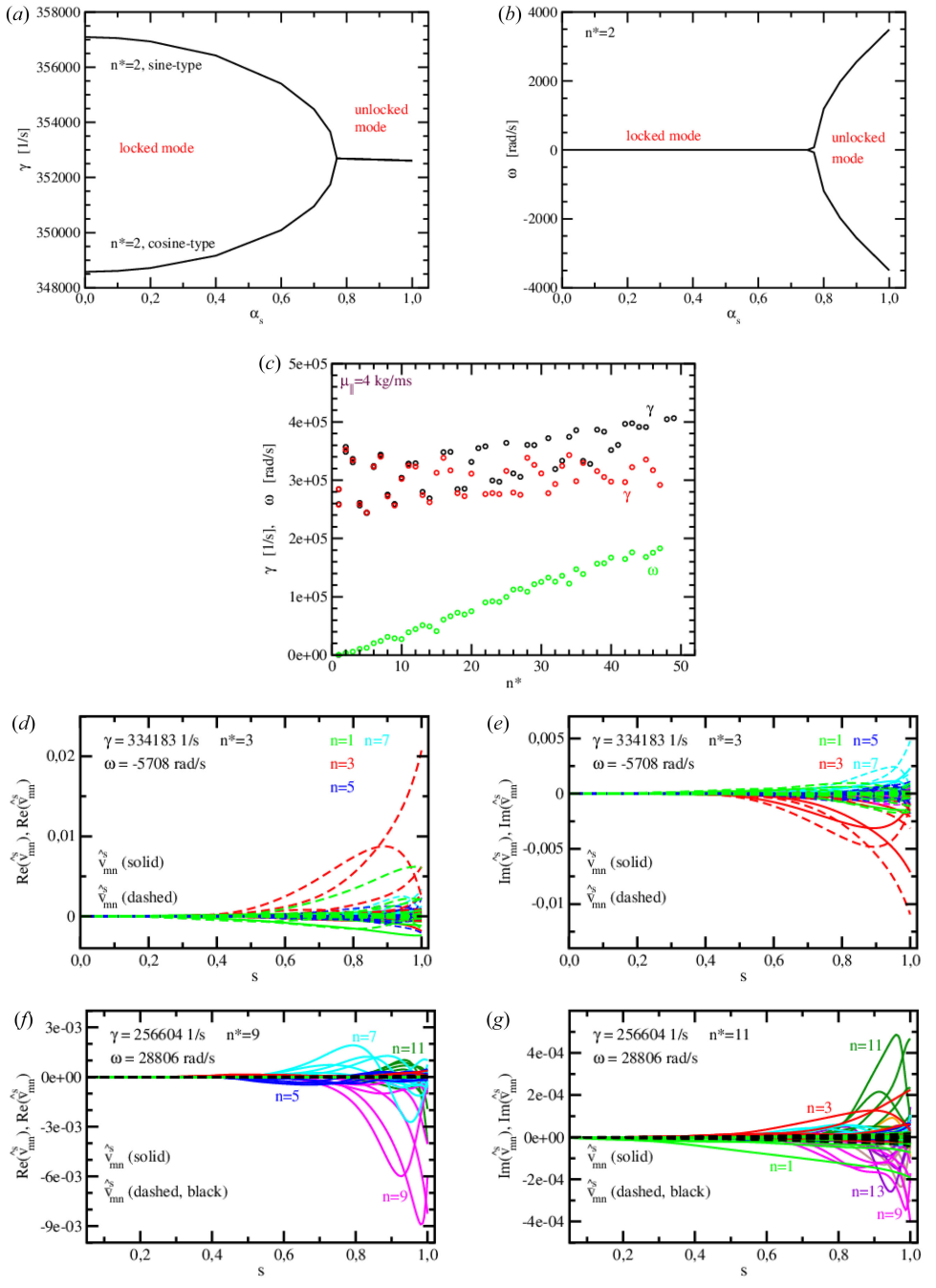


FIGURE 5. Taking parallel and gyro-viscosity into account, (*a*) growth rates and (*b*) oscillation frequencies as functions of the scaling parameter α_s are shown for the $n^* = 2$ external kink modes. (*c*) Growth rates (red circles) and oscillation frequencies (green circles) as functions of n^* in comparison with the growth rates obtained without gyro-viscosity (black circles). Eigenfunction Fourier spectra of the (*d*,*f*) real and (*e*,*g*) imaginary parts of the radial velocity perturbation for the (*d*,*e*) $n^* = 3$ and the (*f*,*g*) $n^* = 9$ external kink modes.

https://doi.org/10.1017/S0022377825101013 Published online by Cambridge University Press

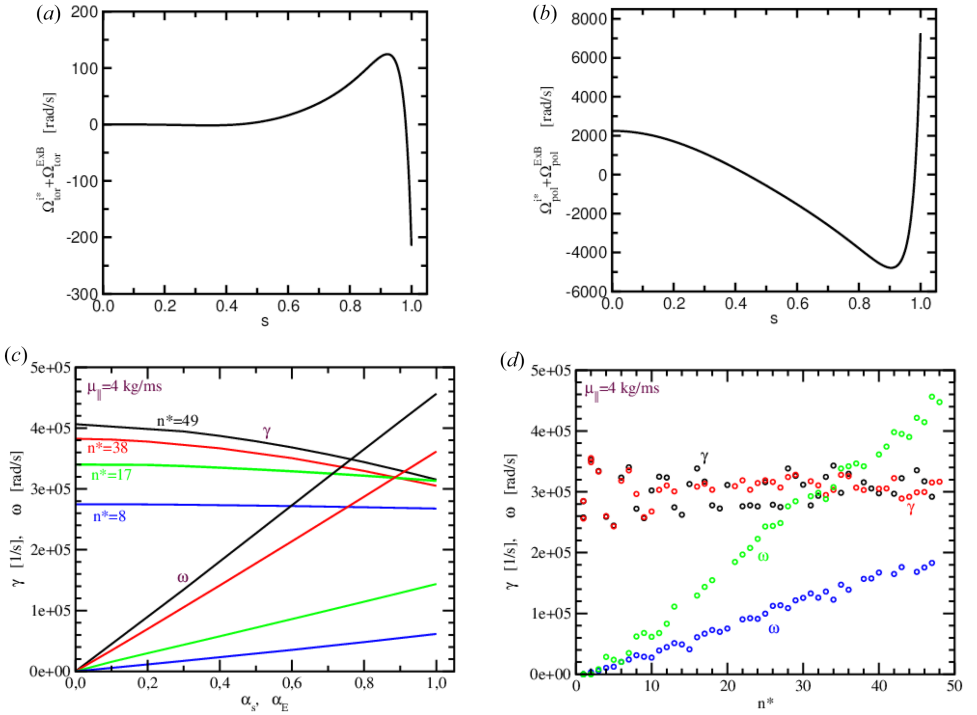


FIGURE 6. (*a*) Toroidal and (*b*) poloidal rotational frequency profiles resulting from the sum of ion drift frequency $\Omega^{i*}(s)$ (figures 1*d* and 1*e*) and $\Omega^{ExB}(s)$-frequency (figures 2*b* and 2*c* (red curves)) in Boozer coordinates. (*c*) Growth rates and oscillation frequencies as functions of the scaling parameters α_s and α_E for various n^*. (*d*) Growth rates and oscillation frequencies as functions of n^* taking parallel and gyro-viscosity into account. The results with and without additional ion diamagnetic and *ExB* velocities are marked by red/green and black/blue circles, respectively.

Comparing real and imaginary parts of the $n^* = 9$ mode (figures 5*f* and 5*g*), we see that the real part is dominated by the $n = 9$ harmonic, while the imaginary part has a larger contribution from the $n = 11$ harmonic. This means that the structure of this mode additionally oscillates between $n^* = 9$ and $n^* = 11$. Since, its real part of the Fourier spectrum is approximately 10 times large than its imaginary part, we classify this mode as an $n^* = 9$ mode.

3.3. *Plasma flows*

Adding up the frequencies of the ion diamagnetic drift velocity (3.1) and the *ExB* velocity (3.4) obtained from the hypothetical electric field, we get the toroidal and poloidal rotational frequencies shown in figures 6(*a*) and 6(*b*). Scaling the gyro-viscosity and these frequencies with the scaling parameters α_s and α_E[5] simultaneously from zero to one results in a decrease of the growth rates and an almost linear increase of the mode frequencies, as shown for a few representative modes in figure 6(*c*). Growth rates and oscillation frequencies are given as functions of n^* and $\alpha_s = \alpha_E = 1$ in figure 6(*d*). In order to point out the effect of the ion diamagnetic

[5]The scaling factor α_E has been implemented into the CASTOR3D code to scale $\boldsymbol{E}_0$.

https://doi.org/10.1017/S0022377825101013 Published online by Cambridge University Press

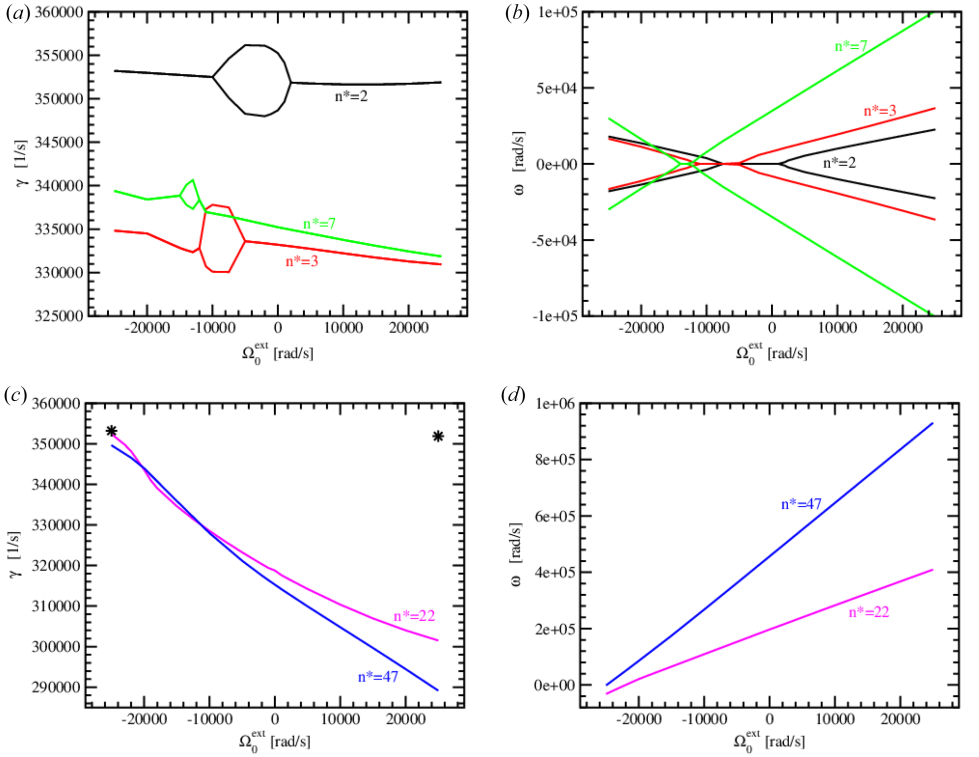


FIGURE 7. (*a*,*c*) Growth rates and (*b*,*d*) oscillation frequencies of (*a*,*b*) $n^* = 2$, 3 and 7 external kink modes, and (*c*,*d*) $n^* = 22$ and 47 peeling-ballooning modes as functions of the externally driven toroidal flow frequency Ω_0^{ext} taking into account parallel viscosity ($\mu_{||} = 4\,\mathrm{kg\,ms^{-1}}$) and gyro-viscosity, as well as, ion diamagnetic drift velocity and *Ex*B velocity. (*a*,*b*) The two solutions per n^* have been obtained by solving the full eigenvalue problem, while the single solutions of (*c*,*d*) have been obtained by solving the reduced eigenvalue problem. (*c*) The two black stars located in the left and right corners mark growth rates of the $n^* = 2$ mode.

drift velocity and *Ex*B velocity, the results obtained without them are also shown in figure 6(*d*). While the velocities increase the oscillation frequencies by a factor of roughly 2.3, they have almost no effect on the growth rates in the case of the considered QA equilibrium.

Finally, we study the influence of parallel viscosity, gyro-viscosity, ion diamagnetic drift velocity and *Ex*B velocity as in the previous case plus a toroidal velocity, $\boldsymbol{V}_{tor}^{ext} = (1/2\pi)\Omega_{tor}^{ext}\boldsymbol{r}_v$, externally driven in the symmetry direction v (Boozer toroidal coordinate) of the equilibrium. We assume $\Omega_{tor}^{ext}(s) = \Omega_0^{ext}(1 - 0.8s^4)$ with $-25\ 000 \leqslant \Omega_0^{ext} \leqslant 25\ 000$ rad s^{-1}. Figure 7(*a–d*) shows the resulting growth rates and oscillation frequencies as functions of the externally driven frequency Ω_0^{ext} for the low-n^* external kink modes $n^* = 2$, 3 and 7 and the high-n^* peeling-ballooning modes $n^* = 22$ and 47. Depending on the sign of Ω_0^{ext}, the additional external drive increases or decreases the damping effect caused by the gyro-viscosity, ion diamagnetic drift velocity and *Ex*B velocity, and also changes the oscillation frequencies of the modes. The growth rate decreases if the chosen flow direction leads to an increase of the oscillation frequency of the mode and *vice versa*. This behaviour is in good agreement with the results obtained by Aiba (2016). Using the MINERVA-DI code, he

https://doi.org/10.1017/S0022377825101013 Published online by Cambridge University Press

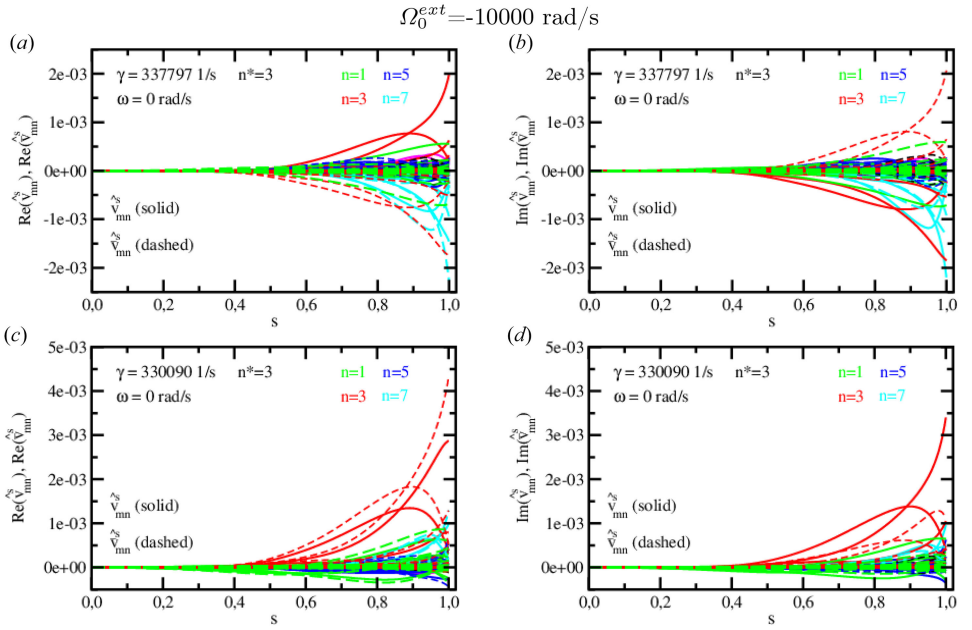


FIGURE 8. (*a*,*c*) Real and (*b*,*d*) imaginary parts of the eigenfunction Fourier spectra given for the radial velocity perturbation of the two $n^* = 3$ modes.

investigated axisymmetric equilibria with circular cross-section. Yet, an additional effect appears in the case of the considered 3-D equilibria. Appropriate external flow compensates the oscillation frequencies caused by gyro-viscosity, diamagnetic drift velocity and *E*x*B* velocity and locks the low-n^* modes again. But, these locked modes are not pure sine- and cosine-type modes, as illustrated by the eigenfunction Fourier spectra of the $n^* = 3$ modes in figure 8(*a–d*).

As already mentioned in previous sections, the classification of rotating modes becomes more and more difficult with increasing n^*. In figures 6(*c*) and 7(*a–d*), we marked the curves by the most represented n^*-values. Although the oscillation frequencies grow almost perfectly linearly, the mode type may change slightly. That is, n^* may vary within a small range of neighbouring values. Figure 9(*a–f*) illustrates this behaviour for the $n^* = 47$ curves in figures 7(*c*) and 7(*d*). The figures show the real and imaginary parts of the eigenfunction Fourier spectra of the high-n^* peeling-ballooning mode for $\Omega_0^{ext} = -25\,000$, 0 and 25 000 rad s^{-1}. Its n^*-values are listed separately for real and imaginary parts of the Fourier spectra. However, the mode is characterised by the dominant part, that is, the n^* values of the real parts of the considered examples. So, the mode type varies between $n^* = 47$ and 49. Furthermore, figure 9(*a–f*) provides some information about the radial extension of the mode. It shrinks with decreasing growth rate and increasing oscillation frequency, that is, the mode becomes more localised at the plasma boundary.

Finally, the presented results show that direction and magnitude of the external flow may decide whether a low-n^* external kink or a high-n^* peeling-ballooning mode will be the most unstable mode. In figure 7(*c*), the black stars mark the growth rates of the $n^* = 2$ mode for $\Omega_0^{ext} = -25\,000$ and 25 000 rad s^{-1}, respectively. Here, the growth rate of the $n^* = 22$ mode has almost reached the value of the $n^* = 2$ mode for $\Omega_0^{ext} = -25\,000$ rad s^{-1}. That is, an external flow in the negative v-direction and

https://doi.org/10.1017/S0022377825101013 Published online by Cambridge University Press

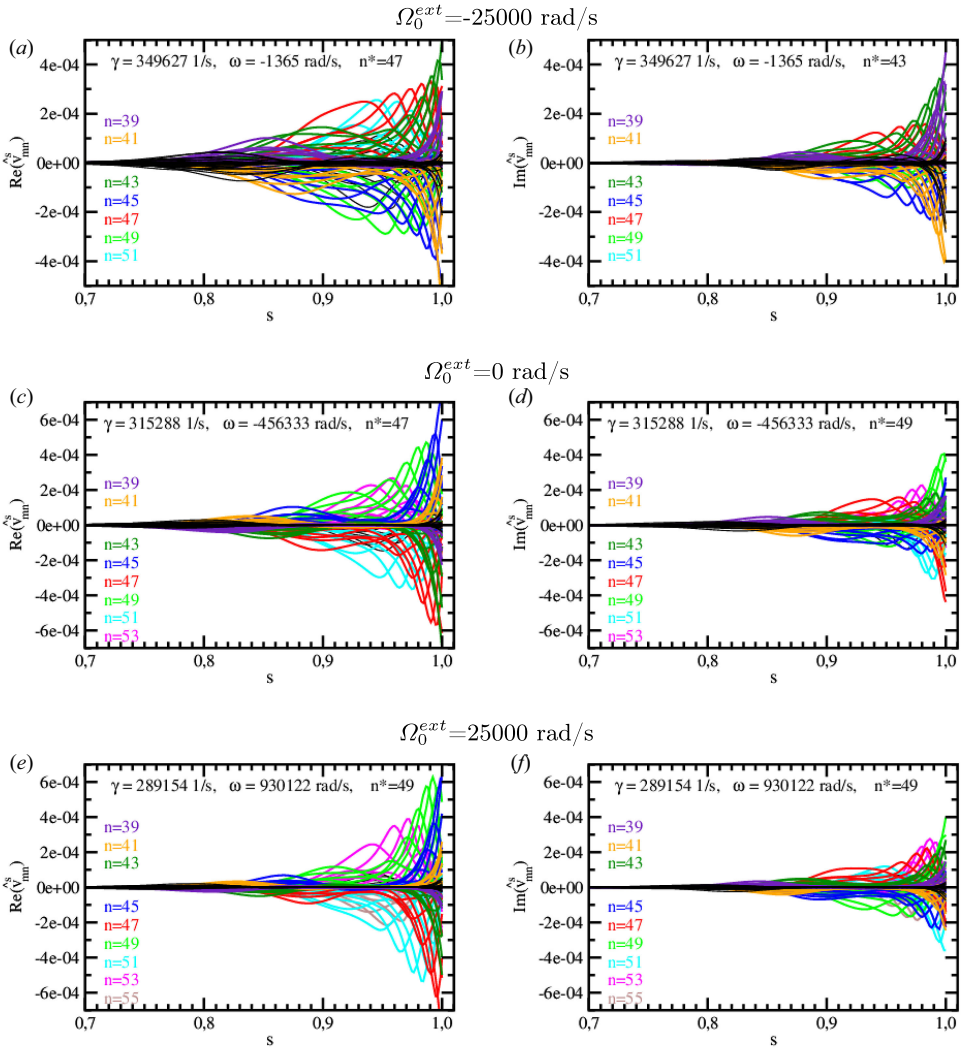


FIGURE 9. (*a*,*c*,*e*) Real and (*b*,*d*,*f*) imaginary parts of the eigenfunction Fourier spectra given for the radial velocity perturbation.

of sufficient magnitude is able to compensate the stabilising effect of gyro-viscosity, ion diamagnetic velocity and *E*x*B* velocity on the high-n^* peeling-ballooning modes and to make them to the most unstable modes of the considered equilibrium, while the growth rates of low-n^* modes are only weakly affected by the flows (see figures 6*d* and 7*a*).

4. Summary

Several numerical improvements of the CASTOR3D code, increased computer power and a highly accurate equilibrium provided by the GVEC code enable high-n^* extended MHD stability studies for stellarator equilibria. In the case of spatially extended low-n^* modes, there is a strong coupling of the $e^{2\pi i(mu+nv)}$ and $e^{-2\pi i(mu+nv)}$ parts of the eigenfunction (A1) which may lead to two solutions with different growth

https://doi.org/10.1017/S0022377825101013 Published online by Cambridge University Press

rates, that is, a slow- and a fast-growing locked mode. However, with increasing n^* the modes become more and more localised and the coupling of two eigenfunction parts becomes negligible. Then, the solution of the reduced eigenvalue problem is sufficient, which enables a further increase of the number of Fourier harmonics and radial grid points to be used for its solution.

Solving the pure ideal eigenvalue problem, the growth rates increase with rising n^*, while parallel viscosity reduces both the growth rates and their increase with n^*. Besides, the parallel viscosity may change the mode type, but it does not induce mode oscillations and, therefore, does not unlock modes. However, sufficiently large gyro-viscosity, ion diamagnetic drift velocity, ExB velocity and/or external flow lead to mode oscillations. They are able to equal otherwise non-degenerate eigenvalues and to unlock the corresponding low-n^* modes, while high-n^* modes are always unlocked. Depending on the direction of an externally driven flow, it may strengthen or weaken the stabilising effects of gyro-viscosity, ion diamagnetic drift velocity and ExB velocity, and even lock low-n^* modes if it leads to a compensation of the oscillations caused by those effects.

Summarising the physical results, the presented stability studies illustrate the need for including the effects of parallel viscosity, gyro-viscosity, ion diamagnetic drift velocity, ExB velocity and externally driven flows because their individual and common impacts are important to determine the stability properties of a given plasma configuration. In case of the considered test equilibrium, they decide whether a low-n^* external kink or a high-n^* peeling-ballooning mode will be the most unstable mode.

Acknowledgements

Editor Per Helander thanks the referees for their advice in evaluating this article.

Funding

This work has been carried out within the framework of the EUROfusion Consortium, funded by the European Union via the Euratom Research and Training Programme (Grant Agreement No 101052200 – EUROfusion). Views and opinions expressed are, however, those of the author(s) only and do not necessarily reflect those of the European Union or the European Commission. Neither the European Union nor the European Commission can be held responsible for them. Open access funding provided by Max Planck Society.

Declaration of interest

The authors report no conflict of interest.

Appendix A

The CASTOR3D code solves a non-Hermitian eigenvalue problem. The ansatz for the complex eigenfunctions reads (Strumberger & Günter 2017)

$$\begin{aligned}\hat{w}_f(s,v,u) &= \sum_{m,n,j,q} a^{s,m,n}_{f,j,q} h^j_{f,q}(s)\sin(2\pi(mu+nv)) + a^{c,m,n}_{f,j,q} h^j_{f,q}(s)\cos(2\pi(mu+nv)) \\ &= \sum_{m,n,j,q} c^{m,n}_{f,j,q} h^j_{f,q}(s) e^{2\pi i(mu+nv)} + \bar{c}^{m,n}_{f,j,q} h^j_{f,q}(s) e^{-2\pi i(mu+nv)}, \end{aligned} \tag{A1}$$

https://doi.org/10.1017/S0022377825101013 Published online by Cambridge University Press

with $\hat{w}_f$ being the components of the state vector $\boldsymbol{w} = (\hat{\rho}, \hat{v}^s, \hat{v}^u, \hat{v}^v, \hat{T}, \hat{A}_s, \hat{A}_u, \hat{A}_v)$, $h^j_{f,q}(s)$ being either quadratic ($f = \hat{\rho}, \hat{v}^u, \hat{v}^v, \hat{T}, \hat{A}_s$) or cubic ($f = \hat{v}^s, \hat{A}_u, \hat{A}_v$) Hermite polynomials[6] and $\{c^{m,n}_{f,j,q}, \bar{c}^{m,n}_{f,j,q}\}$ being the complex Fourier coefficients of the eigenfunctions. They are related with the complex coefficients $\{a^{c,m,n}_{f,j,q}, a^{s,m,n}_{f,j,q}\}$ via

$$a^{c,m,n}_{f,j,q} = \left(c^{m,n}_{f,j,q} + \bar{c}^{m,n}_{f,j,q}\right) \quad \text{and} \quad a^{s,m,n}_{f,j,q} = i\left(c^{m,n}_{f,j,q} - \bar{c}^{m,n}_{f,j,q}\right). \tag{A2}$$

Here, m and n are the poloidal and toroidal Fourier harmonics of the perturbation spectrum, while $q = 1, 2$ labels the two quadratic and the two cubic Hermite polynomials at the radial grid point j (Kerner *et al.* 1998). The ansatz of the full eigenfunction (A1) is needed for low-n^* modes where the $c^{m,n}_{f,j,q}$ and $\bar{c}^{m,n}_{f,j,q}$ parts are strongly coupled and the eigenvalues of the two corresponding solutions are different. However, the coupling between the two parts decreases with increasing n^*, so that the ansatz (A1) can be reduced to

$$\hat{w}_f(s, v, u) = \sum_{m,n,j,q} c^{m,n}_{f,j,q} h^j_{f,q}(s) e^{2\pi i(mu+nv)}, \tag{A3}$$

that is, the matrix size of the eigenvalue problem is reduced by a factor of four.

While in the case of axisymmetric configurations the modes can be easily characterised by their toroidal mode number n, in 3-D plasmas several n-harmonics couple together. Therefore, we introduced the dominant toroidal harmonic n^* to name the modes (Strumberger & Günter 2019). Since, the Fourier spectra of the eigenfunctions reveal important information about the location and structure of a mode, we plot the real and/or imaginary parts of the radial velocity perturbation vicariously for all perturbed quantities. Solving the full eigenvalue problem, the Fourier spectra consist of two parts

$$\hat{v}^s_{m,n}(s) = \sum_{j,q} c^{m,n}_{\hat{v}^s,j,q} h^j_{\hat{v}^s,q} \quad \text{and} \quad \hat{\bar{v}}^s_{m,n}(s) = \sum_{j,q} \bar{c}^{m,n}_{\hat{v}^s,j,q} h^j_{\hat{v}^s,q}. \tag{A4}$$

For example, figures 3(*b*) and 3(*c*) show the $n^* = 4$ mode. In this case, the dominating n-harmonic can be easily identified by considering the spectra. Unfortunately, the identification of the mode type is not always so easy, and with increasing n-harmonics contributing to the mode, it becomes more and more difficult. Therefore, we compute the following four functions:

$$f_{\mathrm{Re}}(n) = \sum_m \int \left(\mathrm{Re}\left(\hat{v}^s_{m,n}(s)\right)\right)^2 \mathrm{d}s, \qquad \bar{f}_{\mathrm{Re}}(n) = \sum_m \int \left(\mathrm{Re}\left(\hat{\bar{v}}^s_{m,n}(s)\right)\right)^2 \mathrm{d}s, \tag{A5}$$

$$f_{\mathrm{Im}}(n) = \sum_m \int \left(\mathrm{Im}\left(\hat{v}^s_{m,n}(s)\right)\right)^2 \mathrm{d}s, \qquad \bar{f}_{\mathrm{Im}}(n) = \sum_m \int \left(\mathrm{Im}\left(\hat{\bar{v}}^s_{m,n}(s)\right)\right)^2 \mathrm{d}s, \tag{A6}$$

and look for their maxima. In case of the considered stellarator-symmetric equilibrium, we have to discriminate between the following cases:

[6]Only cubic Hermite polynomials have to be used if gyro-viscosity in combination with plasma velocity is taken into account because additional first derivatives of Hermite polynomials are needed.

https://doi.org/10.1017/S0022377825101013 Published online by Cambridge University Press

(i) Non-oscillating modes ($\omega = 0$):

(a) sine-type modes ($\hat{v}^s_{m,n}(s) = -\hat{\bar{v}}^s_{m,n}(s)$) and cosine-type modes ($\hat{v}^s_{m,n}(s) = \hat{\bar{v}}^s_{m,n}(s)$) with $Re(\hat{v}^s_{m,n}(s)) = cIm(\hat{v}^s_{m,n}(s))$, $Re(\hat{\bar{v}}^s_{m,n}(s)) = cIm(\hat{\bar{v}}^s_{m,n}(s))$ and $c \in \mathbb{R}$ (see figures 3*b* and 3*c*);

(b) arbitrary-type modes $\hat{v}^s_{m,n}(s) \neq \hat{\bar{v}}^s_{m,n}(s)$ (see figure 8*a–d*).
The maxima of all four functions (A5, A6) are located at the same $n = n^*$.

(ii) Overstable modes ($\omega \neq 0$): sine-type modes ($\hat{v}^s_{m,n}(s) = -\hat{\bar{v}}^s_{m,n}(s)$) and cosine-type modes ($\hat{v}^s_{m,n}(s) = \hat{\bar{v}}^s_{m,n}(s)$) with $Re(\hat{v}^s_{m,n}(s)) \neq Im(\hat{v}^s_{m,n}(s))$ and $Re(\hat{\bar{v}}^s_{m,n}(s)) \neq Im(\hat{\bar{v}}^s_{m,n}(s))$. Equations (A5) and (A6) yield different n^*-values. The mode oscillates between the two n^*-types (see figures 4*e* and 4*f*).

(iii) Rotating modes ($\omega \neq 0$): $\hat{v}^s_{m,n}(s) \neq \hat{\bar{v}}^s_{m,n}(s)$ (see figures 5*d* and 5*e*). With increasing n^* either the $\hat{v}^s_{m,n}(s)$ or the $\hat{\bar{v}}^s_{m,n}(s)$-part disappears depending on the sign of the oscillation frequency. The rotating mode changes its mode type within an oscillation cycle (see figures 5*f* and 5*g*) if the real (A5) and imaginary parts (A6) yield different n^*-values. Usually, we use the larger value to characterise the mode type.

REFERENCES

AIBA, N. 2016 Impact of ion diamagnetic drift on ideal ballooning mode stability in rotating tokamak plasmas. *Plasma Phys. Control. Fusion* **58**, 045020.

ANDERSON, D.V., COOPER, W.A., GRUBER, R., MERAZZI, S. & SCHWENN, U. 1990 Methods for the efficient calculation of the (MHD) magnetohydrodynamic stability properties of magnetically confined fusion plasmas. *Intl J. Supercomput. Appl.* **4**, 34.

BOOZER, A.H. 1982 Establishment of magnetic coordinates for a given magnetic field. *Phys. Fluids* **25**, 520.

BRAGINSKII, S.I. 1965 Transport processes in a plasma. In *Reviews of Plasma Physics* (ed. Leontovich), vol. I, p. 205. Consultants Bureau.

CHANG, Z. & CALLEN, J.D. 1992 Generalized gyroviscous force and its effect on the momentum balance equation. *Phys. Fluids B: Plasma Phys.* **4**, 1766.

CHAPMAN, I.T., SHARAPOV, S.E., HUYSMANS, G.T.A. & MIKHAILOVSKII, A.B. 2006 Modelling the effect of toroidal plasma rotation on drift-magnetohydrodynamic modes in tokamaks. *Phys. Plasmas* **13**, 062511.

GOODMAN, A.G., CAMACHO MATA, K., HENNEBERG, S.A., JORGE, R., LANDREMAN, M., PLUNK, G.G., SMITH, H.M., MACKENBACH, R.J.J., BEIDLER, C.D. & HELANDER, P. 2023 Constructing precisely quasi-isodynamic magnetic fields. *J. Plasma Phys.* **89**, 905890504.

HELANDER, P. & SIMAKOV, A.N. 2008 Intrinsic ambipolarity and rotation in stellarators. *Phys. Rev. Lett.* **101**, 145003.

HENNEBERG, S.A., DREVLAK, M., NÜHRENBERG, C., BEIDLER, C.D., TURKIN, Y., LOIZU, J. & HELANDER, P. 2019 Properties of a new quasi-axisymmetric configuration. *Nucl. Fusion* **59**, 026014.

HINDENLANG, F., BABIN, R., MAJ, O., RIBEIRO, T., KOEBERL, R., MUIR, D., PLUNK, G. & SONNENDRÜCKER, E. 2025*a* GVEC: a flexible 3D MHD equilibrium solver. *Zenodo*. Available at: https://doi.org/10.5281/zenodo.15026781.

HINDENLANG, F., PLUNK, G.G. & MAJ, O. 2025*b* Computing MHD equili*b*ria of stellarators with a flexible coordinate frame. *Plasma Phys. Control Fusion* **67**, 045002.

HIRSHMAN, S.P. & WHITSON, J.C. 1983 Steepest-descent moment method for three-dimensional magnetohydrodynamic equilibria. *Phys. Fluids* **26**, 3553–3568.

HUYSMANS, G.T.A., GOEDBLOED, J.P. & KERNER, W. 1993 Free boundary resistive modes in tokamaks. *Phys. Fluids B* **5**, 1545.

https://doi.org/10.1017/S0022377825101013 Published online by Cambridge University Press

KERNER, W., GOEDBLOED, J.P., HUYSMANS, G.T.A., POEDTS, S. & SCHWARZ, E. 1998 CASTOR: normal-mode analysis of resistive MHD plasmas. *J. Comput. Phys.* **142**, 271.

KERNER, W., JAKOBY, A. & LERBINGER, K. 1986 Finite-element semi-discretization of linearized compressible and resistive MHD. *J. Comput. Phys.* **66**, 332.

LIU, Y.Q., BONDESON, A., FRANSSON, C.M., LENNARTSON, B. & BREITHOLTZ, C. 2000 Feedback stabilization of nonaxisymmetric resistive wall modes in tokamaks. I. Electromagnetic model. *Phys. Plasmas* **7**, 3681.

LIU, Y., CHU, M.S., CHAPMAN, I.T. & HENDER, T.C. 2008 Toroidal self-consistent modeling of drift kinetic effects on the resistive wall mode. *Phys. Plasmas* **15**, 112503.

NIKULSIN, N., RAMASAMY, R., HOELZL, M., HINDENLANG, F., STRUMBERGER, E., LACKNER, K. & GÜNTER, S. 2022 JOREK3D: an extension of the JOREK nonlinear MHD code to stellarators. *Phys. Plasmas* **29**, 063901.

NÜHRENBERG, C. 1996 Global ideal magnetohydrodynamic stability analysis for the configurational space of Wendelstein 7–X. *Phys. Plasmas* **3**, 2401–2410.

NÜHRENBERG, C. 2016 Free-boundary ideal MHD stability of W7-X divertor equilibria. *Nucl. Fusion* **56**, 076010.

NÜHRENBERG, C. 2021 Ideal magnetohydrodynamic stability in stellarators with subsonic equilibrium flow. *Plasma Phys. Control. Fusion* **63**, 125035.

NÜHRENBERG, J., LOTZ, W. & GORI, S. 1994 Quasi-axisymmetric tokamaks. In *Theory of Fusion Plasmas, ISPP-15. Proceeding of Joint Varenna-Lausanne International Workshop*, p. 3.

NÜHRENBERG, J. & ZILLE, R. 1988 Quasi-helically symmetric toroidal stellarators. *Phys. Lett. A* **129**, 113–117.

PATIL, S.A. & SOVINEC, C.R. 2024 Benchmarking of NIMSTELL for tearing modes in stellarators and preconditioner improvements. *Bull. Am. Phys. Soc.* **P12**.

PUCHMAYR, J. 2023 Magnetohydrodynamic stability analysis of non-axisymmetric tokamak plasmas using the linear visco-resistive stability code CASTOR3D. PhD thesis, Fakultät für Physik der Ludwig-Maximilians-Universität München.

PUCHMAYR, J., DUNNE, M., STRUMBERGER, E., WILLENSDORFER, M., ZOHM, H., HINDENLANG, F. & the ASDEX Upgrade Team 2023 Helical mode localization and mode locking of idea MHD instabilities in magnetically perturbed tokamak plasmas. *Nucl. Fusion* **63**, 086008.

PUCHMAYR, J., DUNNE, M., STRUMBERGER, E., WILLENSDORFER, M., ZOHM, H., HINDENLANG, F. & the ASDEX Upgrade Team 2024 Effect of symmetry-breaking on the MHD edge stability limit of tokamak plasmas. *Nucl. Fusion* **64**, 086013.

RAMASAMY, R., ALEYNIKOVA, K., NIKULSIN, N., HINDENLANG, F., HOLOD, I., STRUMBERGER, E., HOELZL, M. & the JOREK team 2024 Nonlinear MHD modeling of soft β limits in W7-AS. *Nucl. Fusion* **64**, 086030.

SPONG, D.A., HIRSHMAN, S.P., LYON, J.F., BERRY, L.A. & STRICKLER, D.J. 2005 Recent advances in quasi-poloidal stellarator physics issues. *Nucl. Fusion* **45**, 918.

STROTH, U., MANZ, P. & RAMISCH, M. 2011 On the interaction of turbulence and flows in toroidal plasmas. *Plasma Phys. Control. Fusion* **53**, 024006.

STRUMBERGER, E. & GÜNTER, S. 2017 CASTOR3D: linear stability studies for 2D and 3D tokamak equilibria. *Nucl. Fusion* **57**, 016032.

STRUMBERGER, E. & GÜNTER, S. 2019 Linear stability studies for a quasi-axisymmetric stellarator configuration including effects of parallel viscosity, plasma flow, and resistive walls. *Nucl. Fusion* **59**, 106008.

STRUMBERGER, E., GÜNTER, S., LACKNER, K. & PUCHMAYR, J. 2023 CASTOR3D: linear magnetohydrodynamics and diamagnetic drift effects. *J. Plasma Phys.* **89**, 905890309.

STRUMBERGER, E., GÜNTER, S. & the Wendelstein 7-X team 2020 Linear, resistive stability studies for Wendelstein 7-X-type equilibria with external current drive. *Nucl. Fusion* **60**, 106013.

VIEZZER, E. 2012 Radial electric field studies in the plasma edge of ASDEX Upgrade. PhD thesis, Fakultät für Physik der Ludwig-Maximilians-Universität München.

WARMER, F. *et al.* 2024 Overview of European efforts and advances in Stellarator power plant studies. *Fusion Eng. Des.* **202**, 114386.

https://doi.org/10.1017/S0022377825101013 Published online by Cambridge University Press